Journal of Materials Chemistry A

ROYAL SOCIETY OF CHEMISTRY

PAPER

View Article Online
View Journal

Cite this: DOI: 10.1039/c9ta13497b

Ultrafast cation insertion-selected zinc hexacyanoferrate for 1.9 V K–Zn hybrid aqueous batteries†

Meng Huang,[a] Jiashen Meng,[a] Zijian Huang,[a] Xuanpeng Wang [b] and Liqiang Mai *[a]

Received 10th December 2019
Accepted 12th February 2020

DOI: 10.1039/c9ta13497b

rsc.li/materials-a

The low energy/power density of aqueous rechargeable batteries (ARBs) have limited their further development and application because of their voltage limitation of 1.23 V. Herein, K–Zn hybrid ARBs with a high discharge voltage of 1.937 V are reported for the first time. The selective ionic insertion/extraction mechanism into/from the zinc hexacyanoferrate (ZnHCF) cathode in the hybrid electrolyte was clearly revealed by *in situ* X-ray diffraction. The cathode material displays an outstanding rate capability of 300C and a high capacity of 78.7 mA h g^{-1}. The constructed K–Zn hybrid ARBs exhibit an energy density of 67 W h kg^{-1}, a high power density of 4.76 kW kg^{-1} and excellent rate performance with 67.6% capacity retention from 2C to 60C. These excellent performances contribute to the selected K^+ insertion mechanism. These exciting results can offer an alternative path for the development of hybrid aqueous batteries for stable and high energy/power density energy storage techniques.

1. Introduction

The global energy crisis is growing and the abuse of fossil fuel aggravates climate change.[1] Thus, countries have spark plugged the large-scale usage of green and renewable energy from wind and solar power but the efficient storage and transport of green energy is a significant challenge.[2,3] For massive energy storage apparatuses, safe operation matters most and low cost, long service life and high efficiency should also be considered.[4–6] Non-aqueous lithium-ion batteries (LIBs) and sodium-ion batteries (SIBs) possess considerable energy densities and exhibit high energy efficiency, while they suffer from hidden safety concerns from flammable organic electrolytes and dendrite formation.[7,8] Besides, the relatively high cost also limits their applications in large-scale energy storage.[9,10] As for high market-share lead-acid cells, although cost-saving, they exhibit undesirable cyclability and poor rate performance.[11] In contrast, aqueous rechargeable batteries (ARBs) arise as alternative candidates for massive energy storage because of their preponderances: (1) high safety, (2) low cost, and (3) environmental benignity.[12–14]

From their first introduction in 1994, ARBs have received increasing attention.[15] Due to the electrolysis of H_2O molecules, the feasible working voltage window for ARBs is limited to approximately 1.23 V, meaning low energy/power density.[13] To break this limitation, the electrolysis of H_2O at the interface of the electrode and electrolyte must be suppressed.[16,17] A fabricated TiO_2//$LiMn_2O_4$ battery exhibited a discharge plateau at 2.09 V because of the effectively suppressed hydrogen and oxygen evolution, but it performed poorly at a low rate for the increased hydrogen evolution during cycling.[18] Prussian blue analogues (PBAs) with stable three-dimensional ionic channels have shown superiority as cathode materials for aqueous rechargeable SIBs and potassium ion batteries (PIBs).[19–22] Cai *et al.* found that high-quality iron hexacyanoferrate nanotubes as cathode materials showed capacity retention of 96.3% after 200 cycles at 1.25 A g^{-1} for aqueous SIBs.[23] Impressively, Ren *et al.* achieved ultrafast potassium-ion insertion/extraction into/from the K-rich mesoporous nickel ferrocyanide cathode in 1 M KNO_3 aqueous electrolytes.[24] This cathode could complete one charge or discharge within 4.1 s, corresponding to an extraordinary rate of 500C, and it presented a long lifetime (>5000 cycles) with a capacity retention of 98.6%. It was also found that PBAs were promising hosts for the insertion/extraction of multivalent cations. A 1.7 V high-voltage aqueous zinc ion battery has been developed[25] and an aqueous magnesium ion battery with a maximum cell voltage of 1.5 V has been constructed;[26] PBAs also show that they are promising hosts for aluminum ions in aqueous electrolytes.[27]

Hybrid ion batteries can combine the respective advantages of two electrode materials with different electrochemistry. Lu

[a]State Key Laboratory of Advanced Technology for Materials Synthesis and Processing, School of Materials Science and Engineering, Wuhan University of Technology, Wuhan 430070, P. R. China. E-mail: mlq518@whut.edu.cn

[b]Department of Physical Science & Technology, School of Science, Wuhan University of Technology, Wuhan 430070, P. R. China

† Electronic supplementary information (ESI) available. See DOI: 10.1039/c9ta13497b

et al. constructed a Na–Zn hybrid aqueous battery that showed a working voltage of approximately 1.5 V and an energy density of 62.9 W h kg^{-1}.[28] To further improve the energy/power and rate performance of the aqueous batteries, new electrochemical energy storage systems need to be studied. It is known that K^+ has greater insertion potential than Na^+ and the zinc anode possesses a low redox potential at approximately −0.78 V.[25,29–31] Moreover, compared with hydrated sodium ions, the smaller Stokes radius of hydrated potassium ions endows aqueous PIBs with better rate performance.[32] Thus, it is supposed that a K–Zn hybrid ion battery possesses a high working voltage and considerable rate ability.

In this work, we propose a high energy/power density K–Zn hybrid ion battery *via* controlled ionic insertion for the first time, based on a zinc hexacyanoferrate (ZnHCF) cathode and a zinc foil anode. In the discharge process at 2C (1C = 86 mA g^{-1}), the ZnHCF cathode shows a flat and long plateau at 0.928 V and a short one at 0.749 V *vs.* the saturated calomel electrode (SCE) derived from K^+ insertion. The insertion of K^+ contributes a capacity of 78.7 mA h g^{-1} of which 60% was maintained at an extraordinarily high rate of 300C. Based on the low redox potential of the zinc anode, the constructed ZnHCF//Zn cell presents high discharge plateaus of 1.937 V at 2C and 1.80 V at 60C. Furthermore, the ZnHCF//Zn cell (the mass ratio of ZnHCF to Zn is ∼1 : 1) showed a high energy density of 67 W h kg^{-1}, and the highest power density can reach 4.76 kW kg^{-1}. This new energy storage chemistry system shows much promise for large-scale energy storage applications.

2. Experimental section

2.1 Material synthesis

In the synthesis of ZnHCF, 50 mL of solution containing 1.8903 g $Zn(NO_3)_2 \cdot 6H_2O$ was added to a 100 mL solution containing 1.27 g $K_3Fe(CN)_6 \cdot H_2O$, drop by drop under stirring at 60 °C for 2 h.[25] After the reaction was complete, the obtained solution was aged for several hours. The precipitate was collected by centrifugation and washed three times with water and pure ethanol, respectively. The washed solid product was dried at 100 °C for over 12 h.

2.2 Material characterization

The morphology was observed by using field emission scanning electron microscopy (SEM, JEOL JSM-7100F, acceleration voltage: 15 kV). Transmission electron microscopy (TEM), high-resolution TEM (HRTEM) images and high angle annular dark-field (HAADF) images were collected by using a Titan G2 60-300 instrument with image corrector. The powder X-ray diffraction (XRD) and *in situ* XRD experiments were performed using a Bruker D8 Discover X-ray diffractometer with a non-monochromated Cu Kα X-ray source. For *in situ* XRD measurements, the positive electrode was covered by a titanium foil with a small hole that was covered with tape. The signals were received by the planar detector in still mode during the testing process. The positive electrodes were fresh and each pattern took 90 s to acquire at 2C charge and 1C discharge. TGA was performed on an STA-449C Thermobalance in an Ar atmosphere with a temperature ramp of 10 °C min^{-1}. Inductively coupled plasma-optical emission spectroscopy (ICP-OES) was performed on a PerkinElmer Optima 4300DV spectrometer.

2.3 Electrochemical measurements

The cathode electrode paste film was prepared by the mixing of active materials, Ketjen black, and polyvinylidene fluoride (7 : 2 : 1). The paste film was dried for at least 12 h at 70 °C and pressed onto the Ti mesh. The mass loading of the active material was 4–5 mg cm^{-2}. The electrochemical measurements of the individual electrode samples and full cell were carried out in a three-electrode cell setup (the paste film on Ti mesh as the working electrode, SCE as the reference electrode and a Pt plate as the counter-electrode) and a two-electrode cell setup (the paste film on Ti mesh as the working electrode and a Zn plate as the counter and reference electrode) in $ZnSO_4/K_2SO_4$ series hybrid electrolytes using an electrochemical workstation (CHI 760E/605E). Galvanostatic charge/discharge tests of the assembled ZnHCF//Zn coin cell with a mass ratio of active materials of 1 : 1 with 2016 coin cells were conducted by using the LAND CT2001A multichannel battery testing system. The Whatman glass microfiber filter (Grade GF/A) was used as the separator. The electrochemical impedance spectroscopy was evaluated by using an electrochemical workstation (CHI 760E).

3. Results and discussion

ZnHCF was synthesized *via* a simple coprecipitation method and the crystal structure was confirmed by powder X-ray Rietveld refinement (Fig. 1a).[33] The crystal structure of ZnHCF is rhombohedral in the group of *R*-3*C* and with lattice parameters of $a = 12.6148$ Å and $c = 33.0495$ Å. Fig. S1† displays the final

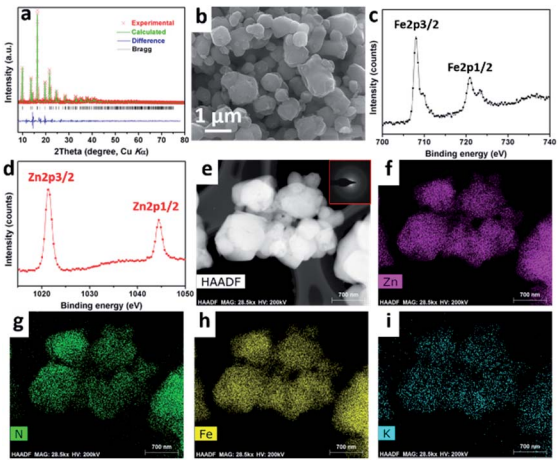

Fig. 1 (a) Powder X-ray Rietveld refinement profile for ZnHCF at 25 °C (red points, experimental pattern; green line, calculated pattern; black bars, Bragg positions; blue line, difference between the experimental and calculated patterns). (b) SEM image of the as-prepared ZnHCF powder. (c) Fe 2p and (d) Zn 2p XPS spectra of ZnHCF. (e) HAADF image of the as-prepared ZnHCF powder (inset is SAED pattern). (f–i) The corresponding EDS mapping images of ZnHCF.

refined structure and the structural parameters are summarized in Table S1.† Through ICP-OES, the molar ratio of K : Zn : Fe in the as-prepared ZnHCF sample was detected to be 0.336 : 2.486 : 2.000 (Table S2†). Thus, the chemical formula of the ZnHCF sample can be assumed to be $K_{0.336}Zn_{2.486}[Fe(CN)_6]_2 \cdot xH_2O$. Thermal gravimetric analysis (TGA) was performed to determine the water content in the ZnHCF sample as $K_{0.336}Zn_{2.486}[Fe(CN)_6]_2 \cdot 3.09H_2O$ (Fig. S2†). The SEM image (Fig. 1b) reveals the ZnHCF has a particle size in the range of 0.5–1.0 μm. From the TEM image (Fig. 1e), the nanoparticles present an irregular shape, indicating the unintegrated characteristics of the crystals. The selected area electron diffraction (SAED) pattern (inset of Fig. 1e) further revealed that the as-prepared ZnHCF sample has a polycrystalline characteristic.[34] The energy-dispersive X-ray (EDX) spectrum (Fig. S3†) and HAADF images (Fig. 1f–i) of the ZnHCF sample show the existence and uniform distribution of N, Fe, Zn, and K elements. X-ray photoelectron spectroscopy (XPS) was further utilized to confirm the presence and valence of Fe and Zn elements. In the high-resolution XPS spectrum (Fig. 1c), the binding energies of Fe $2p_{3/2}$ and Fe $2p_{1/2}$ are situated at approximately 709.7 and 723.3 eV, respectively, indicating that the chemical state of Fe in ZnHCF is the +3 oxidation state, while the two peaks observed at 708.0 and 721.1 eV are derived from $[Fe^{II}(CN)_6]^{4-}$.[25,35] Zn $2p_{3/2}$ and Zn $2p_{1/2}$ peaks located at approximately 1021.4 and 1044.5 eV (Fig. 1d) reveal the presence of Zn^{2+} in ZnHCF.[36] Additionally, according to the integrated counts calculated from the curves of Zn $2p_{3/2}$ and Fe $2p_{3/2}$, the atomic ratio for Zn : Fe is 1.263 : 1, which coincides with the results of ICP-OES.

Electrochemical behaviors of the ZnHCF cathode in various electrolytes were studied by cyclic voltammetry (CV) (Fig. 2a). In 0.05 M $ZnSO_4$ + 0.5 M K_2SO_4 hybrid electrolyte, the ZnHCF cathode presents a strong and sharp cathodic peak at 1.93 V and two small ones at 1.82 and 1.79 V (black curve). During the anodic process, a strong and sharp peak at 2.07 V and a small one at 1.81 V were observed. It is obvious that the peak at 1.79 V pairs that at 1.81 V, while the one at 1.93 V pairs with that at 2.07 V. The anodic peak pairing the cathodic peak at 1.79 V is probably located at 2.01 V. With the increase in $ZnSO_4$ concentration from 0.05 to 0.25 M, the ZnHCF cathode presents a strong and sharp cathodic peak at 1.90 V and two small ones at 1.80 and 1.77 V (magenta curve). During the anodic process, the main peak at 2.05 V and a small peak at 1.78 V were observed. In the 0.25 M $ZnSO_4$ + 0.25 M K_2SO_4 hybrid electrolytes, the ZnHCF cathode shows a couple of strong and sharp redox peaks at 1.87/2.05 V and a small couple at 1.74/1.77 V (dark yellow curve). With the 0.5 M $ZnSO_4$ + 0.25 M K_2SO_4 hybrid electrolytes (electrolyte I), two strong peaks at 1.88 and 1.79 V and a small one at 1.62 V were present during the cathodic process (dark cyan curve). A strong and sharp peak at 2.04 V and a small peak at 1.77 V appeared during the anodic process. It was found that with the concentration of $ZnSO_4$ increasing to 0.5 M and greater than that of K_2SO_4, the second cathodic peak showed enhanced intensity and area. When the concentration of $ZnSO_4$ was fixed at 0.5 M, decreasing the concentration of K_2SO_4 to 0.05 M resulted in the decrease of the first cathodic peak intensity/area at 1.86 V and the increase of the second one at 1.74 V (red curve). The third cathodic peak appeared at 1.55 V, and only one obvious anodic peak at 2.04 V was seen. In the systematic analysis, as the ratio of $ZnSO_4$ to K_2SO_4 increased, the intensity and position of the first cathodic peak weakened and shifted to a lower voltage, while the second cathodic peak became stronger and larger; the anodic peak appeared weaker in intensity, with greater width and at a lower position. The third

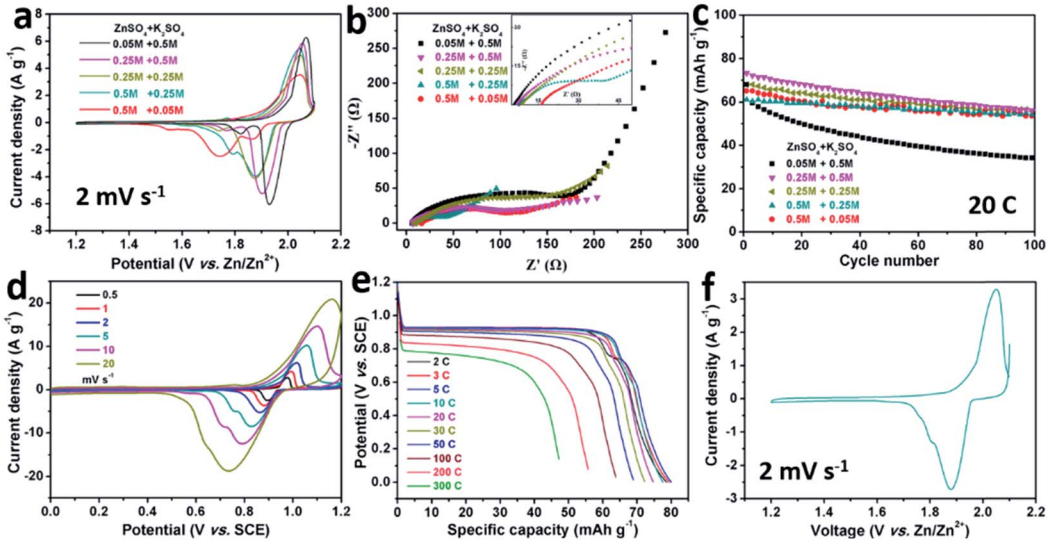

Fig. 2 (a) Cyclic voltammetry curves of ZnHCF in different electrolytes using a three-electrode cell setup (Zn plates were employed as the reference and counter electrodes). (b) EIS and (c) cycling performance of ZnHCF in different electrolytes using a two-electrode cell setup (a Zn plate was employed as the anode). (d) Cyclic voltammetry curves and (e) discharge profiles of ZnHCF in electrolyte I using a three-electrode cell setup (saturated calomel electrode and a Zn plate were employed as the reference and counter electrodes, respectively). (f) Cyclic voltammetry curve of ZnHCF in electrolyte I using a two-electrode cell setup (Zn plate was employed as the anode).

cathodic peak, showed negligible changes as the ratio of $ZnSO_4$ to K_2SO_4 increased. The electrochemical behaviors were, therefore, greatly influenced by the composition of the electrolytes. In addition, it was inferred that the K^+ insertion was supposed to introduce the first cathodic peak, and the second anodic peak at 1.74 V was possibly derived from the Zn^{2+} insertion.[25,28,37]

In the electrochemical impedance spectroscopy (EIS) test in different electrolytes, the same ZnHCF cathode and Zn plate anode were used to ensure the compatibility of the data. A much lower charge transfer resistance (R_{ct}) of 39 Ω was observed for ZnHCF in electrolyte I as compared to other electrolytes (Fig. 2b). Thus, the ZnHCF cathode is expected to present superior electrochemical performance in electrolyte I.[38] In a two-electrode setup, where ZnHCF and a Zn plate were used as the cathode and anode materials, respectively, the cycling stability of the ZnHCF cathode was tested at 20C in different electrolytes (Fig. 2c). The second cycle cathodic capacities of the ZnHCF cathode in 0.05 M $ZnSO_4$ + 0.5 M K_2SO_4, 0.25 M $ZnSO_4$ + 0.5 M K_2SO_4, 0.25 M $ZnSO_4$ + 0.25 M K_2SO_4, 0.5 M $ZnSO_4$ + 0.25 M K_2SO_4, and 0.5 M $ZnSO_4$ + 0.05 M K_2SO_4 hybrid electrolytes were 60.9, 56.9, 68.0, 61.1 and 64.9 mA h g^{-1}, respectively. After 100 cycles, the corresponding capacity retentions were 49.7%, 76.6%, 82.0%, 88.8% and 82.4%, respectively. The electrolytes at the initial state were clean and transparent, after 100 cycles at 20C, the colors of the 0.05 M $ZnSO_4$ + 0.5 M K_2SO_4 and 0.5 M $ZnSO_4$ + 0.25 M K_2SO_4 changed negligibly (Fig. S4 and S5†). After cycling for 1000 cycles at 50C, the color of the 0.05 M $ZnSO_4$ + 0.5 M K_2SO_4 changed to light yellow while that of 0.5 M $ZnSO_4$ + 0.25 M K_2SO_4 remained almost colorless (Fig. S6†). It was found that the R_{ct} values of the electrode in the three-electrode setup changed negligibly after cycling, even in the case of severe capacity decay (Fig. S4 and S6a†). The ZnHCF phase was well kept and no new phase was detected after cycling (Fig. S7†). In addition, the ZnHCF electrode exhibited more stable cyclability in hybrid electrolytes with 0.5 M $ZnSO_4$ than in other electrolytes. Thus, the slow capacity fading of ZnHCF in the $ZnSO_4$/K_2SO_4 hybrid electrolytes mainly resulted from the dissociation of ZnCHF. We assumed that the capacity fade has a linear relationship with the dissolution of ZnHCF. Therefore, according to the capacity fade rate (Fig. S6a and b†), the dissolution rate of ZnHCF was approximately 0.0690% per cycle in 0.05 M $ZnSO_4$ + 0.5 M K_2SO_4, which is 1.91 times as high as that in 0.5 M $ZnSO_4$ + 0.25 M K_2SO_4 (0.0361% per cycle). The above results demonstrate that the ZnHCF cathode performs best in electrolyte I with a high concentration of $ZnSO_4$.

In a three-electrode setup with electrolyte I, CV and discharge testing of the ZnHCF cathode at different scan rates were conducted (Fig. 2d and e). At 0.5 mV s^{-1}, the coupled peaks of 0.97/0.89 V showed a low polarization of 40 mV and at 20 mV s^{-1}, the polarization reached 210 mV (1.16/0.74 V), indicating that the K^+ insertion/extraction has fast kinetics.[39] The electrochemical kinetic process was analyzed through the general equation as follows:[40]

$$i = av^b \quad (1)$$

The anodic b value is 0.5416 and the cathodic value is 0.5450, indicating that the K^+ insertion/extraction behaviors are determined by the faradaic process (Fig. S8a†). The chemical diffusion coefficients of K^+ calculated by CV tests are 1.12 × 10^{-11} cm^2 s^{-1} and 1.41 × 10^{-11} cm^2 s^{-1} for the anodic and cathodic process, respectively (Fig. S8b†), demonstrating the fast diffusion kinetics of K^+ for the ZnHCF cathode.[41] During the discharge process at 2C, the ZnHCF cathode showed a flat and long plateau at 0.928 V and a short one at a 0.749 V, both derived from K^+ insertion and a high specific capacity of 78.7 mA h g^{-1} was obtained (Fig. 2e). At the extraordinarily high rate of 300C, the capacity was maintained at 47.1 mA h g^{-1}, corresponding to a high capacity retention of 60%. This super high rate capability probably benefited from the fast-ionic diffusion kinetics and the low R_{ct} (Fig. S8 and S9†).[24,40–44] When the ZnHCF cathode was paired with the zinc plate anode as a full cell, the CV curve resembled that in the three-electrode test (Fig. 2f).

The assembled cells with the ZnHCF cathode and zinc plate anode were also tested to evaluate the electrochemical performance of the K–Zn hybrid aqueous batteries. At 10C rate, the cell showed a high specific capacity of 67.8 mA h g^{-1}, which maintained 86.4% after 100 cycles (coulombic efficiency > 97%) (Fig. 3a). At 20C, the cell initially released a capacity of 55.6 mA h g^{-1} (coulombic efficiency > 96%), of which 74.1% was maintained after 500 cycles (Fig. 3b). At various current densities of 2, 5, 10, 20, 30, 50 and 60C, the corresponding discharge capacities are 69.1, 66.7, 63.5, 59.5, 56.1, 50.1 and 46.7 mA h g^{-1}, respectively (Fig. 3c). From 2C to 60C, the capacity retention was as high as 67.6%, and when the cycling rate returned to 2C, 96.7% capacity was retained (Fig. S10†), indicating the excellent rate performance of the ZnHCF//Zn cell.[45] During the discharge process, the cell showed a high discharge plateau of 1.94 V at 2C rate and 1.80 V at 60C rate. The ZnHCF//Zn full battery showed superior capability and a higher discharge plateau as compared to other K and Zn ion aqueous batteries (Table S3†). Based on the charge/discharge profile, the ZnHCF//Zn cell (mass ratio of ZnHCF to Zn is ~1 : 1) exhibited a high energy density of 67 W h kg^{-1} at the power density of

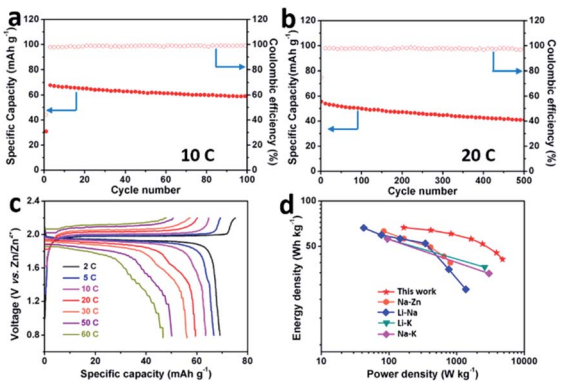

Fig. 3 Cycling performance of ZnHCF//Zn cell at (a) 10C and (b) 20C using a Zn plate anode. (c) Charge/discharge profiles of ZnHCF//Zn (mass ratio of active materials at approximate 1 : 1) cell at different rates. (d) Ragone plot of the ZnHCF//Zn cell measured in (c) and compared with other hybrid ion batteries.

165 W kg^{-1} and the highest power density of 4.76 kW kg^{-1} at the energy density of 41 W h kg^{-1}, which are superior to those reported for Li–Na,[46] Li–K,[47] Na–K[48] and Na–Zn[28] aqueous hybrid ion batteries (Fig. 3d).

The energy storage mechanisms in different electrolytes were further revealed *via in situ* XRD characterizations (Fig. 4). In pure K_2SO_4 electrolyte, the (116) and (211) diffraction peaks shifted in three stages to higher angles because of the formation of $[Fe^{II}(CN)_6]^{4-}$ during the constant K^+ insertion process (Fig. 4a and c).[29,49] In stage I, the shifting slope was constant and the corresponding discharge profile varied in the same mode (Fig. 4a and b). Particularly, in the enlarged stacked diffraction patterns of Fig. 4c, the intensities of the (116) and (211) diffraction peaks shifted to higher angles. The inserted K^+ and the formation of $[Fe^{II}(CN)_6]^{4-}$ caused lattice distortion and in stage II, a larger lattice distortion was induced, which resulted in the increase in the activation energy of K^+ insertion.[37] The two diffraction peaks slowly shifted to higher angles with the insertion of K^+ in stage III. After two integrated charge/discharge cycles, the major diffraction peaks recovered to their original positions, indicating the high reversibility of the insertion/extraction of K^+ (Fig. 4a).[50,51] When tested in pure $ZnSO_4$ electrolyte, the ZnCHF electrode showed different electrochemical behaviors and phase evolution processes (Fig. 4d–f). In stage I, the (116) and (211) diffraction peaks slowly shifted to higher angles (Fig. 4f) due to the lattice distortion caused by Zn^{2+} insertion and the formation of $[Fe^{II}(CN)_6]^{4-}$.[52] The discharge voltage difference between stage II and I also revealed the increased activation energy of Zn^{2+} insertion (Fig. 4e). In stage II, the (116) and (211) diffraction peaks shifted to higher angles and gradually disappeared, while diffraction peaks (1–16) and (2–11) grew and dominated, indicating the crystal structure evolution from rhombohedral to cubic. In stage III, the newly generated diffraction peaks remained in position while the intensity grew stronger with the sustained insertion of Zn^{2+} during further discharge (Fig. 4d). The (116) and (211) diffraction peaks exhibited little offset to lower angles after two cycles, revealing irreversible structural evolution on the insertion/extraction of Zn^{2+}. On comparing the results in pure K_2SO_4 and $ZnSO_4$ electrolytes, it was found that Zn^{2+} with larger charge density introduced phase transformation to ZnCHF while the K^+ insertion process involves a solid–solution intercalation mechanism, which might be caused by the larger charge density of Zn^{2+} as compared to K^+.

In the 0.5 M $ZnSO_4$ + 0.05 M K_2SO_4 hybrid electrolyte, ZnCHF showed two ionic storage mechanisms, the solid–solution intercalation mechanism and two phase-transformation mechanism. During the continuous charge/discharge processes, the (1–16) and (2–11) diffraction peaks gradually emerged, while (116) and (211) diffraction peaks exhibited the same shifting mode as observed in the pure K_2SO_4 electrolyte (Fig. 4g–i). Combined with the CV results (Fig. 2a), it is probable that the insertion of K^+ and the subsequent insertion of Zn^{2+} occurred in the 0.5 M $ZnSO_4$ + 0.05 M K_2SO_4 hybrid electrolyte.[53] When the concentration of K^+ increased from 0.05 M to 0.25 M, the shifting mode of the diffraction peaks resembled that in the pure K_2SO_4 electrolyte (Fig. 4j–l), revealing the selective K^+ insertion/extraction mechanism of ZnCHF in electrolyte I. This controlled K^+ insertion/extraction process was also observed in the other three hybrid electrolytes (Fig. S11†). CV of the same ZnHCF sample was conducted in the pure K_2SO_4 electrolyte (red curve) and $ZnSO_4$ electrolyte (blue curve) at 5 mV s^{-1},

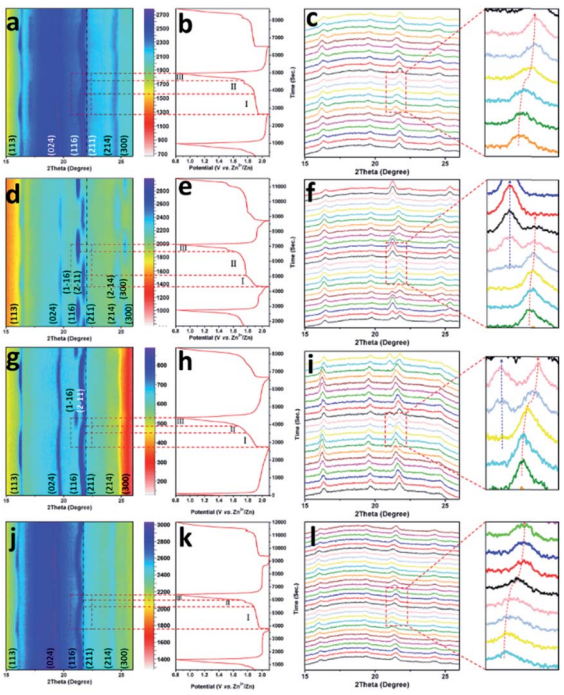

Fig. 4 (a–c) 0.5 M K_2SO_4 electrolyte, (d–f) 0.5 M $ZnSO_4$ electrolyte, (g–i) 0.5 M $ZnSO_4$ + 0.05 M K_2SO_4 electrolyte and (j–l) 0.5 M $ZnSO_4$ + 0.25 M K_2SO_4 electrolyte. (a, d, g and j) 2D XRD patterns; (b, e, h and k) corresponding charge/discharge profiles at a charge rate of 2C and discharge rate of 1C; (c, f, i and l) 1D XRD patterns.

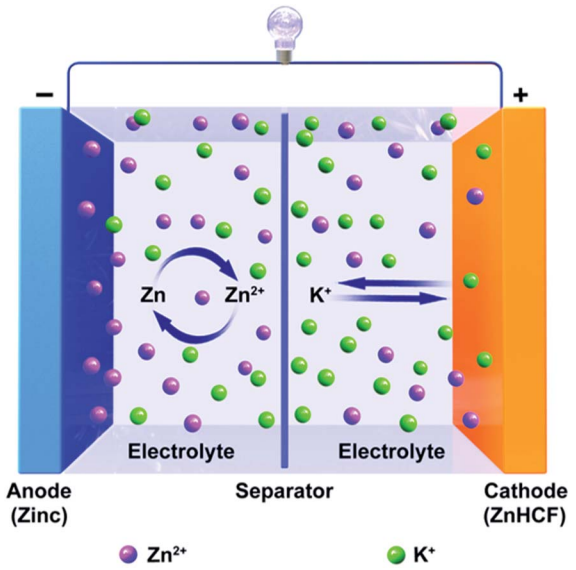

Scheme 1 Schematic illustration of the working principle of the ZnHCF//Zn battery during the charge/discharge processes.

respectively (Fig. S12†). The CV curves showed a much higher redox potential in the former electrolyte than the latter, indicating that K^+ insertion/extraction occurred in thermodynamic preference to Zn^{2+}.[25,37] Nevertheless, the Zn^{2+} insertion occurred in the 0.5 M $ZnSO_4$ + 0.05 M K_2SO_4 hybrid electrolyte, revealing that concentration also affects the ionic insertion/extraction process and confirming the above conjecture. In conclusion, kinetics and thermodynamics act in concert to select the K^+ insertion/extraction and guarantee the better cyclability of the ZnCHF cathode materials (Fig. 2c) and a high discharge voltage of 1.937 V for the ZnHCF//Zn full cell (Fig. 2e). With the electrochemical dissolution/redeposition of the Zn anode (Fig. S13†), the working principle of the ZnHCF//Zn full cell in the 0.5 M $ZnSO_4$ + 0.25 M K_2SO_4 hybrid electrolyte is illustrated in Scheme 1.

4. Conclusions

The ZnHCF cathode demonstrated ultrahigh rate performance of 47 mA h g^{-1} at 300C in mild-hybrid aqueous electrolytes due to fast ionic diffusion kinetics and low impedance, and better cyclability in electrolytes with high concentrations of Zn^{2+}. The selective insertion/extraction of the K^+ mechanism was credibly analyzed and demonstrated by an *in situ* XRD technique. The controlled ionic insertion in hybrid electrochemical chemistry rendered ZnHCF with a high specific capacity of 69 mA h g^{-1} and an excellent rate performance, and a high discharge voltage of 1.937 V for the ZnHCF//Zn full cell. The constructed ZnHCF//Zn cell with the mass ratio of active materials of 1 : 1 had a high density energy of 67 W h kg^{-1} and power density of 4.76 kW kg^{-1}, showing a great potential for ARBs. This K–Zn hybrid electrochemical storage system provides an alternative means for developing high-performance and economical large-scale energy systems.

Conflicts of interest

The authors declare no conflict of interest.

Acknowledgements

This work was supported by the National Natural Science Foundation of China (51832004, 21905218), the Yellow Crane Talent (Science & Technology) Program of Wuhan City, and the Fundamental Research Funds for the Central Universities (WUT: 203114001). We sincerely thanks Dawei Wen (School of Applied Physics and Materials, Wu Yi University, Jiangmen, Guangdong, 529020, China, E-mail: ontaii@163.com) for the powder X-ray Rietveld refinement.

References

1 M. Armand and J. M. Tarascon, *Nature*, 2008, **451**, 652–657.
2 Y. Li, Y. Lu, C. Zhao, Y.-S. Hu, M.-M. Titirici, H. Li, X. Huang and L. Chen, *Energy Storage Mater.*, 2017, **7**, 130–151.
3 S. Chou and Y. Yu, *Adv. Energy Mater.*, 2017, **7**, 1703223.
4 S. Chu, Y. Cui and N. Liu, *Nat. Mater.*, 2016, **16**, 16–22.
5 N. Günter and A. Marinopoulos, *J. Energy Storage*, 2016, **8**, 226–234.
6 K. Liang, L. Li and Y. Yang, *ACS Energy Lett.*, 2017, **2**, 373–390.
7 J. Cui, S. Yao and J.-K. Kim, *Energy Storage Mater.*, 2017, **7**, 64–114.
8 J. F. Peters, M. Baumann, B. Zimmermann, J. Braun, M. J. R. Weil and S. E. Reviews, *Renew. Sust. Energy Rev.*, 2017, **67**, 491–506.
9 G. Martin, L. Rentsch, M. Höck and M. Bertau, *Energy Storage Mater.*, 2017, **6**, 171–179.
10 L. Grandell, A. Lehtilä, M. Kivinen, T. Koljonen, S. Kihlman and L. S. Lauri, *Renew. Energy*, 2016, **95**, 53–62.
11 D. G. Enos, S. R. Ferreira, H. M. Barkholtz, W. Baca and S. Fenstermacher, *J. Electrochem. Soc.*, 2017, **164**, A3276–A3284.
12 L. Suo, F. Han, X. Fan, H. Liu, K. Xu and C. Wang, *J. Mater. Chem. A*, 2016, **4**, 6639–6644.
13 H. Kim, J. Hong, K. Y. Park, H. Kim, S. W. Kim and K. Kang, *Chem. Rev.*, 2014, **114**, 11788–11827.
14 L. Jiang, Y. Lu, C. Zhao, L. Liu, J. Zhang, Q. Zhang, X. Shen, J. Zhao, X. Yu, H. Li, X. Huang, L. Chen and Y.-S. Hu, *Nat. Energy*, 2019, **4**, 495–503.
15 W. Li, J. R. Dahn and D. S. Wainwright, *Science*, 1994, **264**, 1115–1118.
16 C. Yang, J. Chen, T. Qing, X. Fan, W. Sun, A. von Cresce, M. S. Ding, O. Borodin, J. Vatamanu, M. A. Schroeder, N. Eidson, C. Wang and K. Xu, *Joule*, 2017, **1**, 122–132.
17 L. Suo, O. Borodin, W. Sun, X. Fan, C. Yang, F. Wang, T. Gao, Z. Ma and M. Schroeder, *Angew. Chem., Int. Ed.*, 2016, **55**, 7136–7141.
18 S. Liu, S. H. Ye, C. Z. Li, G. L. Pan and X. P. Gao, *J. Electrochem. Soc.*, 2011, **158**, A1490–A1497.
19 C. Liu, X. Wang, W. Deng, C. Li, J. Chen, M. Xue, R. Li and F. Pan, *Angew. Chem., Int. Ed.*, 2018, **57**, 7046–7050.
20 Y. H. Zhu, Y. B. Yin, X. Yang, T. Sun, S. Wang, Y. S. Jiang, J. M. Yan and X. B. Zhang, *Angew. Chem., Int. Ed.*, 2017, **56**, 7881–7885.
21 J.-G. Wang, Z. Zhang, X. Zhang, X. Yin, X. Li, X. Liu, F. Kang and B. Wei, *Nano Energy*, 2017, **39**, 647–653.
22 W. Ren, M. Qin, Z. Zhu, M. Yan, Q. Li, L. Zhang, D. Liu and L. Mai, *Nano Lett.*, 2017, **17**, 4713–4718.
23 D. Cai, X. Yang, B. Qu and T. Wang, *Chem. Commun.*, 2017, **53**, 6780–6783.
24 W. Ren, X. Chen and C. Zhao, *Adv. Energy Mater.*, 2018, **8**, 1801413.
25 L. Zhang, L. Chen, X. Zhou and Z. Liu, *Adv. Energy Mater.*, 2015, **5**, 1400930.
26 L. Chen, J. L. Bao, X. Dong, D. G. Truhlar, Y. Wang, C. Wang and Y. Xia, *ACS Energy Lett.*, 2017, **2**, 1115–1121.
27 S. Liu, G. L. Pan, G. R. Li and X. P. Gao, *J. Mater. Chem. A*, 2015, **3**, 959–962.
28 K. Lu, B. Song, J. Zhang and H. Ma, *J. Power Sources*, 2016, **321**, 257–263.
29 C. D. Wessells, S. V. Peddada, R. A. Huggins and Y. Cui, *Nano Lett.*, 2011, **11**, 5421–5425.

30 J. W. Mccargar and V. D. Neff, *J. Phys. Chem.*, 1988, **92**, 3598–3604.
31 A. B. Bocarsly and S. Sinha, *J. Electroanal. Chem. Interfacial Electrochem.*, 1982, **140**, 167–172.
32 Q. Zhang, H. Chen, T. Wu, T. Jin, Z. Pan, J. Zheng, Y. Gao and W. Zhuang, *Chem. Sci.*, 2017, **8**, 1429–1435.
33 F. Izumi and K. Momma, *Solid State Phenom.*, 2007, **130**, 15–20.
34 S. Xu, Q. Wang, J.-h. Cheng, Q.-h. Meng and Y. Jiao, *Powder Technol.*, 2010, **199**, 139–143.
35 L. Shen, Z. Wang and L. Chen, *Chem.–Eur. J.*, 2014, **20**, 12559–12562.
36 H. Huang, P. Xu, Z. Dan, C. Chen and X. Li, *J. Mater. Chem. A*, 2015, **3**, 6330–6339.
37 Y. Mizuno, M. Okubo, E. Hosono, T. Kudo, H. Zhou and K. Oh-ishi, *J. Phys. Chem. C*, 2013, **117**, 10877–10882.
38 J. L. Yang, S. X. Zhao, Y. M. Lu, X. T. Zeng, W. Lv and G. Cao, *J. Mater. Chem. A*, 2020, **8**, 231–241.
39 F. Cheng, H. Wang, Z. Zhu, W. Yan, T. Zhang, Z. Tao and J. Chen, *Energy Environ. Sci.*, 2011, **4**, 3668–3675.
40 V. Augustyn, J. Come, M. A. Lowe, J. W. Kim, P. L. Taberna, S. H. Tolbert, H. D. Abruna, P. Simon and B. Dunn, *Nat. Mater.*, 2013, **12**, 518–522.
41 T. Brezesinski, J. Wang, S. H. Tolbert and B. Dunn, *Nat. Mater.*, 2010, **9**, 146–151.
42 L. Wang, J. Zhao, X. He, J. Gao, J. Li, C. Wan and C. Jiang, *Int. J. Electrochem. Sci.*, 2012, **7**, 345–353.
43 H. Liu, C. Li, H. P. Zhang, L. J. Fu, Y. P. Wu and H. Q. Wu, *J. Power Sources*, 2006, **159**, 717–720.
44 Z. Jiang, H. Xie, S. Wang, X. Song, X. Yao and H. Wang, *Adv. Energy Mater.*, 2018, **8**, 1801433.
45 A. S. Prakash, P. Manikandan, K. Ramesha, M. Sathiya, J. M. Tarascon and A. K. Shukla, *Chem. Mater.*, 2010, **41**, 2857–2863.
46 Y. Kong, J. Sun, L. Gai, X. Ma and J. Zhou, *Electrochim. Acta*, 2017, **255**, 220–229.
47 P. Jiang, H. Shao, L. Chen, J. Feng and Z. Liu, *J. Mater. Chem. A*, 2017, **5**, 16740–16747.
48 L. Chen, H. Shao, X. Zhou, G. Liu, J. Jiang and Z. Liu, *Nat. Commun.*, 2016, **7**, 11982.
49 A. Dostal, G. Kauschka, S. J. Reddy and F. Scholz, *J. Electroanal. Chem.*, 1996, **406**, 155–163.
50 X. Wang, X. Xu, C. Niu, J. Meng, M. Huang, X. Liu, Z. Liu and L. Mai, *Nano Lett.*, 2017, **17**, 544–550.
51 M. Huang, C. Zhang, C. Han, X. Xu, X. Liu, K. Han, Q. Li and L. Mai, *Electrochim. Acta*, 2017, **254**, 262–268.
52 L. Zhang, L. Chen, X. Zhou and Z. Liu, *Sci. Rep.*, 2015, **5**, 18263.
53 T. Gupta, A. Kim, S. Phadke, S. Biswas, T. Luong, B. J. Hertzberg, M. Chamoun, K. Evans-Lutterodt and D. A. Steingart, *J. Power Sources*, 2016, **305**, 22–29.